

OPEN

Optical Study of the Electronic Structure and Lattice Dynamics of NdBaMn₂O₆ Single Crystals

Rea Divina Mero¹, Kirari Ogawa², Shigeki Yamada² & Hsiang-Lin Liu^{1*}

We investigated the electronic structure and lattice dynamics of double perovskite NdBaMn₂O₆ single crystals through spectroscopic ellipsometry and Raman scattering spectroscopy. The optical absorption band centered at approximately 0.88 eV was assigned to on-site *d–d* transitions in Mn, whereas the optical feature at approximately 4.10 eV was assigned to charge-transfer transitions between the 2*p* state of O and 3*d* state of Mn. Analysis of the temperature dependence of the *d–d* transition indicated anomalies at 290 and 235 K. The activated phonon mode, which appeared at approximately 440 cm^{−1} alongside with the enhancement of the 270 cm^{−1} phonon mode, coupled strongly to the metal–insulator transition at 290 K, which was associated with a charge/orbital ordering. Moreover, the MnO₆ octahedral breathing mode at 610 cm^{−1} exhibited softening at a temperature lower than 235 K (temperature of the antiferromagnetic phase transition), which revealed the strong coupling between the lattice and magnetic degrees of freedom. The spin–phonon coupling constant obtained was $\lambda = 2.5 \text{ cm}^{-1}$. These findings highlight the importance of charge–orbital–spin interactions in establishing NdBaMn₂O₆ phases with novel properties.

Colossal magnetoresistance has promising applications. The search for room-temperature colossal magnetoresistance has resulted in the creation of new perovskite manganites^{1–4}. Perovskite manganites have unique physical properties because of the interactions among the charge, orbital, and spin degrees of freedom^{5–9}. Studies have been conducted extensively on perovskite manganites, which have the general formula $R_{1-x}A_x\text{MnO}_3$ (*R*: rare-earth cation; *A*: alkaline-earth cation)^{10–12}. The random distribution of R^{3+} and A^{2+} causes this system to have inherent disorder in the lattice¹³. This randomness makes it difficult to characterize the effect of lattice distortions on the physical properties. By contrast, double perovskite manganites have an *A*-site ordered structure that eliminates randomness^{14–18}. Their general formula is $Re\text{BaMn}_2\text{O}_6$, where *Re* refers to rare-earth elements, such as Tb, Dy, Ho, Sm, Eu, Gd, La, and Nd. The structure of double perovskite manganites comprises alternately stacked layers of *ReO*, *MnO*₂, and *BaO* along the *c*-axis. This creates a *MnO*₂ square sublattice sandwiched between two types of rock-salt layers (*RO* and *BaO*) with substantially different sizes. Furthermore, $Re\text{BaMn}_2\text{O}_6$ can be classified into three categories according to its crystal structure and the mismatch between the sublattices. Small *Re* elements such as Tb, Dy, Ho, and Y are monoclinic, at room temperature and exhibit large octahedral tilting. *Re* elements such as Sm, Eu, and Gd are tetragonal and exhibit a marginal tilt in the *MnO*₆ octahedra. La, Pr, and Nd also have a tetragonal structure; however, because of their relatively large ions, they exhibit no octahedral tilt at room temperature^{19,20}. Generally, the mismatch between the trivalent *Re* and divalent *Ba* increases the *Mn–O* bond lengths on the *ReO* side and decreases them on the *BaO* side. Moreover, the *Mn–O–Mn* bond angles have a deviation of at least 5° for an angle lower than 180°. The changes in the bond lengths and bond angles decrease the bandwidth^{19,21}.

$Re\text{BaMn}_2\text{O}_6$ has a complex phase diagram, and the phases of $Re\text{BaMn}_2\text{O}_6$ are classified into three groups. The first group has the largest mismatch and exhibits three transitions: a structural transition at high temperature, a charge/orbital-order transition associated with a metal–insulator transition, and an antiferromagnetic transition during cooling. The second group has an ionic radius smaller than Sm and exhibits a CE-type charge/orbital-ordered ground state, which is stable at high temperatures. Moreover, the second group does not exhibit a structural transition. The third group exhibits a ferromagnetic transition as well as a transition from the ferromagnetic state to the *A*-type antiferromagnetic state^{19,21}. Generally, $Re\text{BaMn}_2\text{O}_6$ has a similar phase diagram with the $R_{1-x}A_x\text{MnO}_3$ except that the former has higher charge/orbital-order transition which is stable around the

¹Department of Physics, National Taiwan Normal University, Taipei, 11677, Taiwan. ²Department of Material System Science, Yokohama City University, Yokohama, 236-0027, Japan. *email: hliu@ntnu.edu.tw

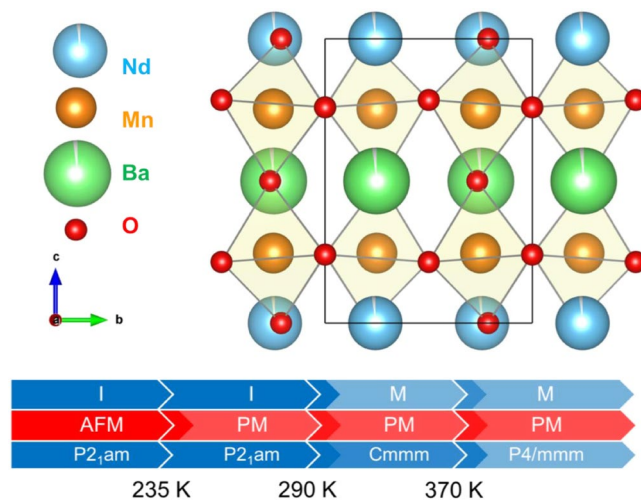


Figure 1. (a) Crystal structure of $\text{NdBaMn}_2\text{O}_6$ at low temperatures²⁸. (b) Schematic depicting the electric, magnetic, and structural transitions occurring in $\text{NdBaMn}_2\text{O}_6$ (M: metallic, I: insulator, AFM: antiferromagnetic, and PM: paramagnetic).

element Nd. The structural transition without charge and magnetic ordering that occurs above the charge/orbital ordering temperature is also unique in $\text{ReBaMn}_2\text{O}_6$.

The properties of the third group of phases are interesting. The rare absence of octahedral tilt in these compounds at room temperature makes them ideal for understanding how it affects phase transitions. The properties of $\text{NdBaMn}_2\text{O}_6$ are also worth investigating because $\text{NdBaMn}_2\text{O}_6$ is located in a critical region between the phase boundaries of the charge/orbital-ordered, A-type antiferromagnetic, and ferromagnetic phases. A strong competition among phases, particularly between the ferromagnetic metal and antiferromagnetic insulator, is crucial for colossal magnetoresistance.

Previous studies have indicated that polycrystalline $\text{NdBaMn}_2\text{O}_6$ has a tetragonal crystal structure with the space group $P4/mmm$ at 400 K^{21–23}. $\text{NdBaMn}_2\text{O}_6$ exhibits a paramagnetic to ferromagnetic metal transition at 300 K, followed by a ferromagnetic to A-type antiferromagnetic metal transition at 290 K²². One study reported the ferromagnetic to antiferromagnetic transition and associated resistivity change to occur at 275 K²¹, whereas another reported its occurrence at 210 K²³. The ferromagnetic to antiferromagnetic transition is associated with a change in the lattice parameters where the *ab*-plane expands and the *c*-axis shortens, which coincides with the charge/orbital ordering^{21,24}. Furthermore, the transitions lead to interesting phenomena observed at approximately room temperature, which increase the functionality of $\text{NdBaMn}_2\text{O}_6$ ^{23,25}.

A detailed understanding of the structural, magnetic, and transport properties of $\text{NdBaMn}_2\text{O}_6$ can be obtained by analyzing isotropic single-crystal^{26,27} and polycrystalline samples. At room temperature, single-crystal $\text{NdBaMn}_2\text{O}_6$ has an orthorhombic structure with a $Cmmm$ space group, and the MnO_6 octahedral exhibits no tilting. At temperatures higher than 370 K, $\text{NdBaMn}_2\text{O}_6$ has a symmetric $P4/mmm$ structure, which is consistent with polycrystalline samples. At temperatures lower than 300 K, MnO_6 octahedra alternately tilt by approximately 5° around the *a*-axis because of the contraction of the *ab*-plane and elongation of the *c*-axis, which coincide with the charge/orbital ordering. This structural transition coupled with the orbital-order transition result in a three-order change in the resistivity of the metal–insulator transition at 290 K. The octahedral tilt increases up to 10° with cooling, which modifies the structure to include the orthorhombic space group $P2_1am$. The direction of the octahedral tilt at low temperatures is 45° from that at 300 K²⁶. Temperature-dependent magnetic susceptibility measurements revealed that the material became antiferromagnetic below $T_N = 235$ K. The crystal structures and phase transitions are summarized in Fig. 1²⁸.

Despite vast research conducted on $\text{NdBaMn}_2\text{O}_6$, its optical and vibrational properties have remained largely unexplored^{21–27}. In this study, we used spectroscopic ellipsometry and Raman scattering spectroscopy to explore the electronic structure and lattice dynamics of $\text{NdBaMn}_2\text{O}_6$. Understanding the intrinsic mechanisms governing the optical and phononic excitations is important for device applications. We also studied the correlation between the temperature-dependent optical response and complex phase transitions of $\text{NdBaMn}_2\text{O}_6$, which helped in elucidating the nature of interactions among the charge, structure, and magnetism in this system and provided a strategy for controlling the functionality of double perovskite manganites.

Experiment

The floating zone method was used to grow single crystals of $\text{NdBaMn}_2\text{O}_6$. The details of sample preparation and characterization are provided in²⁶. The crystals with the (001) surface used in this study had approximate dimensions of $3 \times 3 \times 0.5$ mm³. The spectroscopic ellipsometry measurements were performed under angles of incidence between 60° and 75° using a Woollam M-2000U ellipsometer over a spectral range of 0.73–6.42 eV. For temperature dependent measurements between 4.5 and 500 K, the ellipsometer was equipped with a Janis ST-400 ultrahigh-vacuum cryostat. Due to the 70° angle of the two cryostat windows, only a single angle of incidence is possible. The Raman scattering spectra were measured in a backscattering configuration using a laser with an

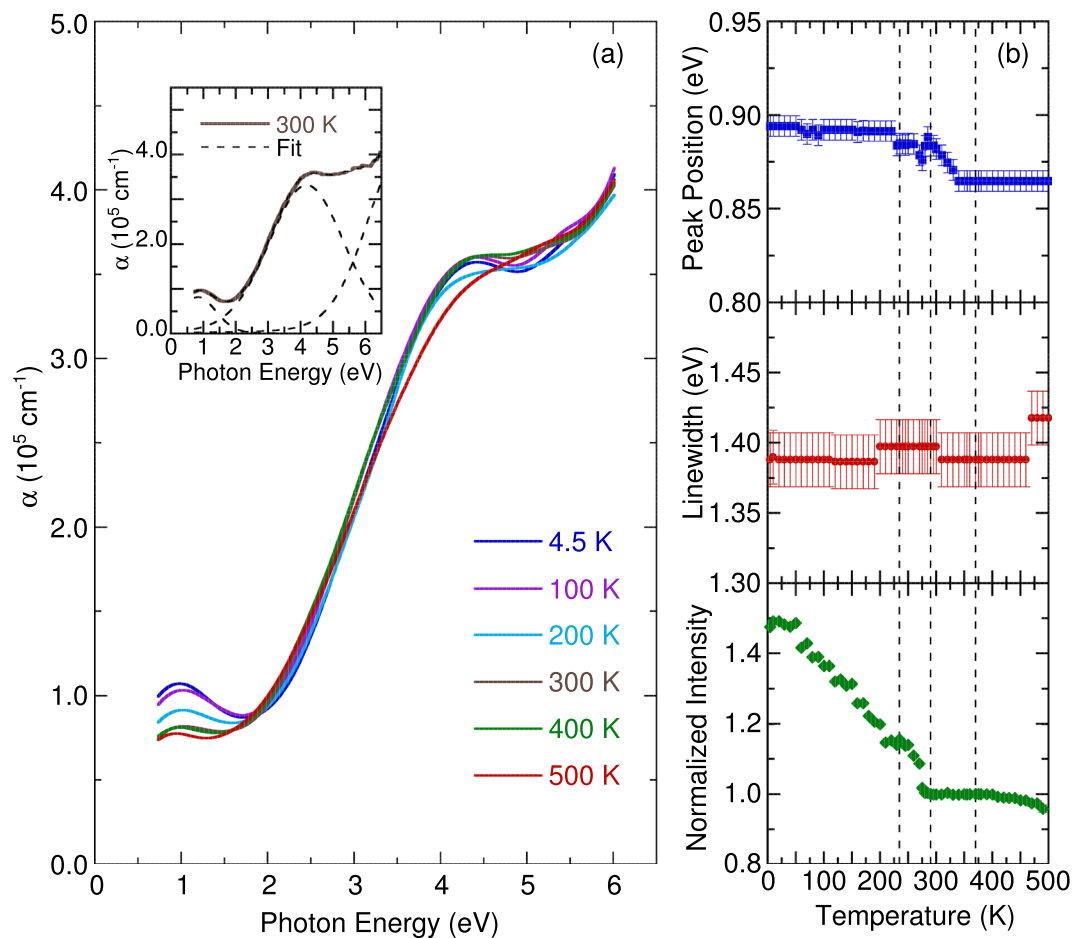


Figure 2. (a) Temperature dependence of the optical absorption spectra of NdBaMn₂O₆. The inset illustrates the best fit with the Lorentz-Gaussian function at 300 K. (b) The temperature dependence of the *d-d* excitation energy, linewidth and normalized intensity. The vertical dashed lines denote the transition temperatures.

excitation wavelength of 532 nm and a SENTERRA spectrometer with a 1024-pixel-wide charge-coupled detector. The incident beam is parallel to the *z*-axis and was kept at 2.0 mW. The polarized Raman scattering spectra were obtained in backscattering geometry from four scattering configurations: Z(Y, Y)Z̄, Z(Y, X)Z̄, Z(Y', Y')Z̄, and Z(Y', X')Z̄. In this Porto notation, the first and the last letter represent the directions of the incident and the scattered light, whereas the letters in parentheses indicate the polarizations of the incident and scattered light, respectively. X, Y, and Z are parallel to the orthorhombic [100], [010], and [001] crystal directions while X' and Y' are along [110] and [1̄10] crystal directions, respectively. The sample was placed in a continuous-flow helium cryostat and LINKAM heating stage, which allowed measurements in the temperature range of 20–500 K. Apart from marginal intensity changes, no significant differences were observed in the spectra obtained at 300 K between the low- and high-temperature set-ups.

Results and Discussion

Electronic excitation. The inset of Fig. 2(a) displays the room temperature optical absorption spectrum of NdBaMn₂O₆ obtained through spectroscopic ellipsometry. The room temperature spectrum were fitted using a Lorentz-Gaussian function, which accounts the broadening at room temperature. The absorption was resolved into two peaks at approximately 0.88 and 4.10 eV. We did not focus on the third band, because its peak exceeded the measured photon energy range. The origin of these peaks was explained using different mechanisms because of the complicated degrees of freedom associated with perovskite manganites. Noh *et al.*²⁹ proposed a model comprising peaks at 1.5 (associated with the interorbital transition in the same Mn³⁺ site) and 4.5 eV (associated with the transition between the 2*p* state of O and the 3*d* state of Mn). This model is based on double exchange and phonon–electron interaction. Accordingly, the peak at 0.88 eV can be assigned to *d-d* excitation. This is similar with the peak observed for SmBaMn₂O₆ at 1.1 eV which was also assigned to *d-d* excitation²¹. Although SmBaMn₂O₆ and NdBaMn₂O₆ are structurally close compounds, the small difference in their size results to large differences in their ground state properties. At room temperature NdBaMn₂O₆ shows metallic properties while SmBaMn₂O₆ is an insulator. Thus, the discrepancy in the observed peak can be explained by the Jahn-Teller effect. It was pointed out that the smaller Sm ions are expected to have a larger mismatch and greater Jahn-Teller distortions resulting to a higher energy peak compared to NdBaMn₂O₆. Previous study on Nd_{0.7}Sr_{0.3}MnO₃³⁰ reported a broad peak at 1.2 eV. This peak was assigned to the charge transfer from Mn³⁺ to Mn⁴⁺, which was most likely caused by the

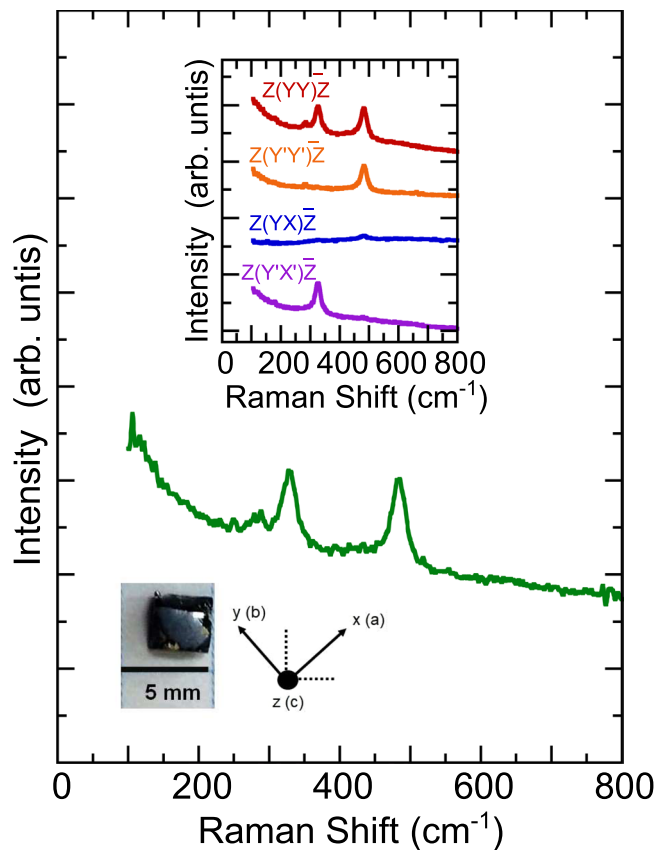


Figure 3. Unpolarized room-temperature Raman scattering spectrum of $\text{NdBaMn}_2\text{O}_6$. The inset illustrates the polarized Raman scattering spectra and the optical image of $\text{NdBaMn}_2\text{O}_6$ single crystal. The notations used for the crystallographic directions are also given.

Jahn–Teller effect coupled with the exchange phenomena. Other studies have also reported the same results^{2,29–33}. At the higher energy range between 2.0 and 5.0 eV, the optical spectrum of $\text{Nd}_{0.7}\text{Sr}_{0.3}\text{MnO}_3$ at 300 K resembles that of $\text{NdBaMn}_2\text{O}_6$. $\text{Nd}_{0.7}\text{Sr}_{0.3}\text{MnO}_3$ features a peak at 4.5 eV due to charge transfer transitions between the O $2p$ and Mn e_g bands³⁰. Parallel to this, the peak at 4.10 eV was assigned to charge-transfer transitions between the $2p$ state of O and $3d$ state of Mn, which is consistent with other perovskite manganites^{2,29–33}. The higher energy bands are well predicted by the ionic model and a common feature in RMnO_3 systems^{34,35}. Insufficient data at energies beyond 2.0 eV for $\text{SmBaMn}_2\text{O}_6$ limits the comparison.

Figure 2(a) illustrates the temperature dependence of the optical absorption spectra. As the temperature decreased, all optical absorptions exhibited shifts of the peak positions to higher energies and narrowing of linewidths. Figure 2(b) denotes the peak energy, linewidth, and normalized intensity of 0.88 eV $d-d$ excitation as a function of temperature. Notably, the $d-d$ excitation energy shows anomalies at 290 and 235 K, accompanied by an enhanced intensity below 290 K. As previously mentioned, below 290 K the charge/orbital ordering develops and $\text{NdBaMn}_2\text{O}_6$ exhibits an insulating behavior^{24,26,27} as the MnO_6 octahedra tilting. The anomalies in energy and intensity are a reflection of how the $d-d$ excitation band captures electrons in the conduction band resulting to a lower conductivity upon cooling. These anomalies below 290 K also emphasize the role of the octahedra tilting on the metal-insulator transition. In addition, the $d-d$ excitation shows discontinuity in the energy and intensity near the 235 K Neel temperature, implying that a change in the electronic structure of $\text{NdBaMn}_2\text{O}_6$ occurs due to the effect of long-range antiferromagnetic ordering. This behavior suggests a strong coupling between the electronic structure and magnetic ordering through charge-spin interactions.

Vibrational properties. Figure 3 displays the room-temperature Raman scattering spectrum of $\text{NdBaMn}_2\text{O}_6$. The spectrum comprises three first-order Raman phonon modes. We fitted these phonon peaks using a standard Lorentzian profile. According to factor group analysis³⁶, $\text{NdBaMn}_2\text{O}_6$ crystallizes with a $Cm\bar{m}m$ orthorhombic structure at 300 K. This structure contains four molecules in the Bravais cell ($Z=4$) located in the $4g$ (Nd), $4h$ (Ba), $8n$ (Mn), $4i$ (O), $4j$ (O), $4k$ (O), $4l$ (O), and $8m$ (O) Wyckoff sites. The motion of the Nd and Ba atoms is represented as $\Gamma_{\text{Nd}} = \Gamma_{\text{Ba}} = A_g + B_{3u} + B_{1g} + B_{2u} + B_{2g} + B_{1u}$. The motion of the Mn atoms can be represented as $\Gamma_{\text{Mn}} = 2A_g + 2B_{3g} + A_u + B_{3u} + B_{1g} + B_{2g} + 2B_{1u} + 2B_{2u}$. Adding the contribution from the O atoms, the irreducible representation of the phonon modes at the center of the Brillouin zone is $\Gamma_{\text{vib}} = 9A_g + 6B_{1g} + 7B_{2g} + 8B_{3g} + 2A_u + 8B_{1u} + 9B_{2u} + 8B_{3u}$. The A_g , B_{1g} , B_{2g} , and B_{3g} modes are Raman active; B_{1u} , B_{2u} and B_{3u} modes are infrared active; and A_u mode is neither Raman nor infrared active. The $\text{NdBaMn}_2\text{O}_6$ structure with the $Cm\bar{m}m$ space group includes 30 Raman-active modes and only $9A_g$ and $6B_{1g}$

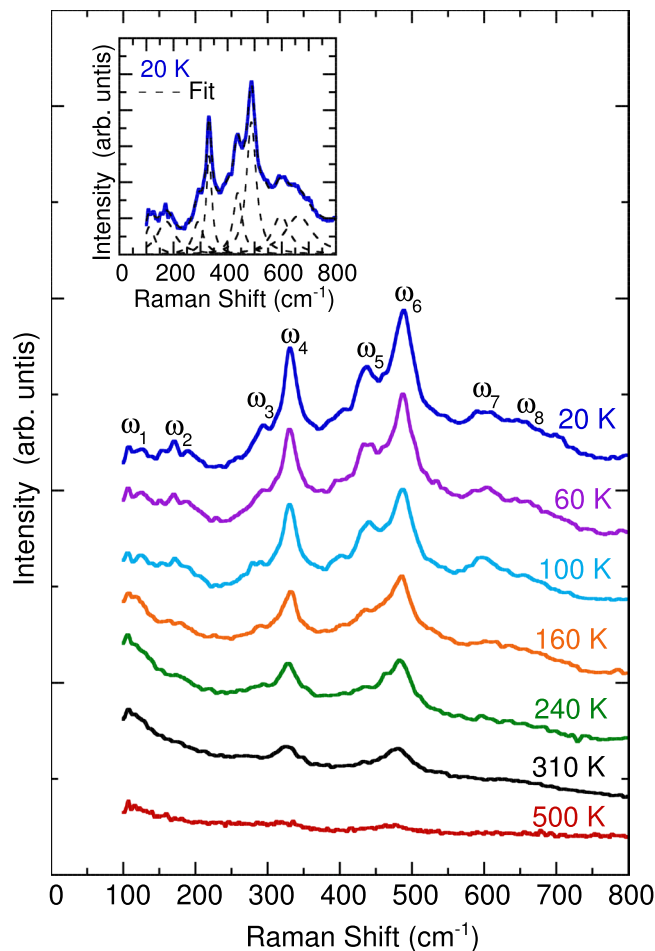


Figure 4. Temperature dependence of the unpolarized Raman scattering spectra of NdBaMn₂O₆. The inset illustrates the results of fitting the spectrum obtained at 20 K by using the Lorentzian model. The background was removed from the linear fits described in the text.

modes are expected considering the crystal orientation adapted. Below 290 K the crystal structure shifts to $P2_1am$. The phonon modes for this structure is given by $\Gamma_{vib} = 16A_1 + 13A_2 + 12B_1 + 16B_2$. The A_1 , B_1 and B_2 are Raman active with $16A_1$ modes expected to be observed in our adapted orientation. At temperatures higher than 370 K, the NdBaMn₂O₆ crystal transitions from an orthorhombic $Cmmm$ structure to a tetragonal $P4/mmm$ structure. There are 18 Γ -point phonon modes for this structure composed of $2A_{1g} + B_{1g} + 5A_{2u} + B_{2u} + 3E_g + 6E_u$. The A_{1g} , B_{1g} , and E_g modes are Raman active which gives a total of six modes. The A_{2u} and E_u modes are infrared active, whereas B_{2u} is a silent acoustic mode. Out of the six Raman-active modes, only three modes composed of two A_{1g} and one B_{1g} are expected in the $P4/mmm$ considering the crystal orientation employed in the study. Additional details of the factor group analysis are provided in the supplementary information.

We observed a total of three Raman-active phonon modes at room temperature. This is consistent with the expected phonon modes for $P4/mmm$. The peaks are composed of two intense modes at approximately 320 and 480 cm^{-1} and a small peak around 270 cm^{-1} . The inset of Fig. 3 displays the polarized Raman scattering spectra in four different configurations. The modes at 270, 320, and 480 cm^{-1} exhibited a higher intensity in the parallel configuration (YY) than in the cross configuration (YX). This satisfies the selection rule for $P4/mmm$ in which A_{1g} and B_{1g} modes should appear in the YY configuration and no peaks are expected for the YX configuration. On the other hand, the primed spectra $Y'Y'$ and $Y'X'$ are different compared to its unprimed counterpart YY and YX which shows that the sample is a single crystal. The $Y'Y'$ spectrum shows the presence of the mode around 480 cm^{-1} and the weak peak around 270 cm^{-1} . The $Y'X'$ spectrum shows the suppressed intensity of the 270 and 480 cm^{-1} phonon modes while exhibiting a strong intensity of phonon mode at 320 cm^{-1} . We can deduce that the 270 and 480 cm^{-1} phonon modes have A_{1g} symmetry while the 320 cm^{-1} phonon mode has B_{1g} symmetry. The 270 cm^{-1} mode was assigned to the octahedral rotation mode and can be used as a measure of octahedral tilting³⁷. The 320 cm^{-1} mode was assigned to MnO₆ octahedral out-of-phase tilting and bending. The 480 cm^{-1} mode was assigned to the Jahn–Teller distortion, which mainly involves symmetric stretching of O atoms. These assignments were parallel to SmBaMn₂O₆²¹ and other perovskite materials^{37–41}. The temperature-dependent Raman scattering spectra of NdBaMn₂O₆ are displayed in Fig. 4. The intensity of the phonon modes weakened when the temperature was increased to 500 K. By contrast, the Raman scattering spectrum exhibited sharp phonon

Frequency (cm ⁻¹)		
ω_1	117	Mixed vibrations from Nd and Ba
ω_2	177	
ω_3	296	Octahedral distortion
ω_4	332	
ω_5	442	Jahn-Teller stretching
ω_6	489	
ω_7	600	Breathing modes
ω_8	653	

Table 1. Raman peaks observed at 20 K with their corresponding symmetry assignments.

Mode	Frequency (cm ⁻¹)			
	NdBaMn ₂ O ₆	SmBaMn ₂ O ₆ ²¹	Nd _{0.5} Sr _{0.5} MnO ₃ ⁴²	La _{0.5} Ca _{0.5} MnO ₃ ⁴³
Mixed mode	272		205	230
Octahedral distortion (tilting/bending/rotation)	327		335 (A)	337
Jahn-Teller stretching	444 (A) 483	496	415 444 489 (A)	473 487
Breathing modes	612 (A) 653 (A)	620	610 (A) 651 (A)	601 643 (A)

Table 2. Raman peaks observed at 280 K for NdBaMn₂O₆ with the corresponding peaks for SmBaMn₂O₆, Nd_{0.5}Sr_{0.5}MnO₃, and La_{0.5}Ca_{0.5}MnO₃. Frequencies labelled with (A) are modes that appear at low temperature.

modes at 20 K. Eight Lorentzian oscillators were used to represent the Raman scattering spectrum at 20 K (inset of Fig. 4), whereas the background was taken to be linear in these fits using the form $A\omega + B$, where A and B are adjustable parameters. The mode frequency and assignment are summarized in Table 1.

Raman scattering spectra of half-doped manganites Nd_{0.5}Sr_{0.5}MnO₃⁴² and La_{0.5}Ca_{0.5}MnO₃⁴³ can be associated with that of NdBaMn₂O₆ which are summarized in Table 2. At 280 K, Raman peaks for Nd_{0.5}Sr_{0.5}MnO₃ are centered around 205, 415, and 444 cm⁻¹ with 335, 489, and 610 cm⁻¹ appearing as temperature was lowered. These peaks also have a counterpart for La_{0.5}Ca_{0.5}MnO₃ at 337, 473, 487 and 601 cm⁻¹. At the same temperature, NdBaMn₂O₆ shows similar peaks at 272, 327, 444 and 483 cm⁻¹. The 327 cm⁻¹ mode for NdBaMn₂O₆ which describes the distortion of the octahedra corresponds to 335 and 337 cm⁻¹ modes for Nd_{0.5}Sr_{0.5}MnO₃ and La_{0.5}Ca_{0.5}MnO₃, respectively. The 444 and 483 cm⁻¹ Jahn-Teller modes corresponds to 415 and 444 cm⁻¹ modes for Nd_{0.5}Sr_{0.5}MnO₃ and 473 and 487 cm⁻¹ modes for La_{0.5}Ca_{0.5}MnO₃. Similar with Nd_{0.5}Sr_{0.5}MnO₃, the breathing mode of NdBaMn₂O₆ at 612 cm⁻¹ also appears when temperature was lowered. The higher frequency breathing mode at 653 cm⁻¹ for NdBaMn₂O₆ was also observed for the half-doped manganites when temperature was lowered. The 205 cm⁻¹ mode for Nd_{0.5}Sr_{0.5}MnO₃ (230 cm⁻¹ mode for La_{0.5}Ca_{0.5}MnO₃) which is associated with the manganite rotation-like mode and also a measure of the average angle of octahedral tilt^{43,44} corresponds to 272 cm⁻¹ mode for NdBaMn₂O₆. This peak appears relatively weak compared to Nd_{0.5}Sr_{0.5}MnO₃ and La_{0.5}Ca_{0.5}MnO₃. This might be due to the layered structure in the A-site ordering. A dramatic enhancement in intensity below 235 K was observed for this peak, indicating the increase in the tilting of the MnO₆ as temperature decreases. Although Raman peaks of half-doped manganites and the A-site ordered manganites have a strong similarity, a number of relatively weak peaks that appear in both Nd_{0.5}Sr_{0.5}MnO₃ and La_{0.5}Ca_{0.5}MnO₃ cannot be accounted in NdBaMn₂O₆. These peaks are centered at 316, 358, 509, 216, 258, 401, and 428 cm⁻¹ in Nd_{0.5}Sr_{0.5}MnO₃⁴² with corresponding peaks at 319, 359, 516, 217, 270, 401, and 429 cm⁻¹ in La_{0.5}Ca_{0.5}MnO₃⁴³. The appearance of these peaks in Nd_{0.5}Sr_{0.5}MnO₃ and La_{0.5}Ca_{0.5}MnO₃ agrees with previous studies^{42,43,45} that these peaks originates from the charge ordering. NdBaMn₂O₆ exhibits charge/orbital ordering reaching up to room temperatures which competes with ferromagnetic interaction²⁴. The charge/orbital ordering melts above room temperature upon the enhancement of the A-site ordering. Based on these comparisons with the half-doped disordered manganites, we can associate A-site ordering signature to less random tilting modes characterize by fewer and distinct Raman peaks below 300 cm⁻¹. Additionally, A-site ordering results to narrower phonon linewidths compared to those of disordered manganites⁴²⁻⁴⁶.

It would also be interesting to compare the counterpart of the peaks in NdBaMn₂O₆ to SmBaMn₂O₆ especially the octahedra tilting mode. Previous study on the Raman scattering spectra of manganites with general formula RMnO₃ reveals that this mode shifts to higher frequency as the ionic radius of the rare earth element decreases⁴⁷. However, the Raman data available in literature is limited only between 350 and 750 cm⁻¹. Still, similar spectral lines observed for SmBaMn₂O₆ at 500 cm⁻¹ Jahn-Teller peak has counterpart in NdBaMn₂O₆ at 490 cm⁻¹ while the breathing mode peak at 620 cm⁻¹ was resolved into two peaks at 600 and 653 cm⁻¹. The slight shift in the frequency in these neighboring compounds can be ascribed to the influence of the bond angle changes brought about by their difference in size.

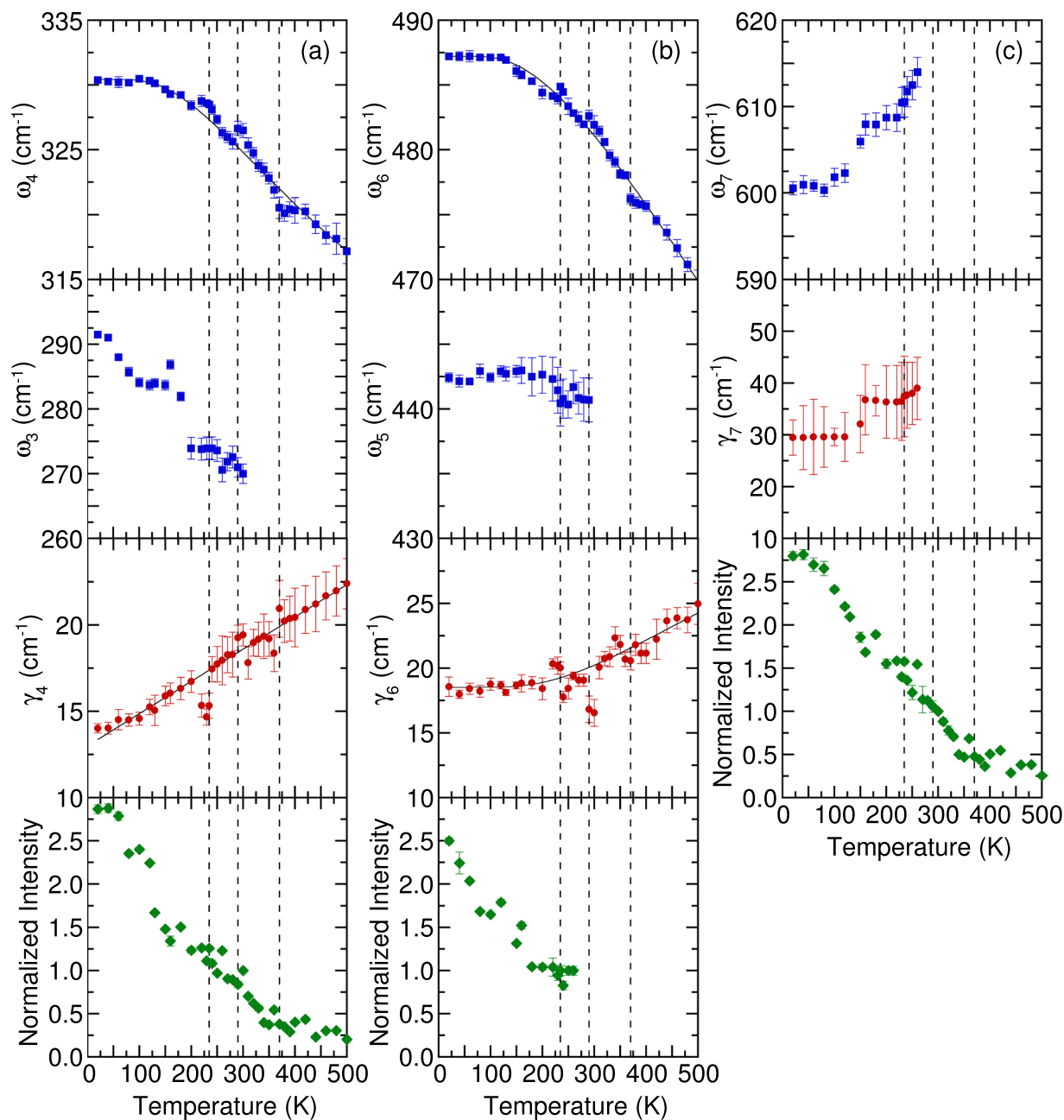


Figure 5. Temperature dependence of the frequency, linewidth, and normalized intensity of the phonon modes. The thin solid lines are the fitting results obtained with the anharmonic model. The vertical dashed lines denote the transition temperatures.

When the temperature decreased, the peak positions of most of the phonon modes of $\text{NdBaMn}_2\text{O}_6$ shifted to higher frequencies, and their resonance linewidth decreased. However, the phonon parameters of the octahedral bending (320 cm^{-1}) and Jahn–Teller (480 cm^{-1}) modes exhibited peculiar behavior at 370 , 290 , and 235 K . A shoulder peak began to appear alongside the strong 480 cm^{-1} mode when the temperature was reduced to less than 290 K while the 270 cm^{-1} mode shows a dramatic enhancement. Moreover, two breathing modes with frequencies higher than 600 cm^{-1} appeared below the magnetic transition temperature ($T_N = 235\text{ K}$). Figure 5 illustrates the peak frequency, linewidth, and normalized intensity of the phonon modes as functions of the temperature. The frequencies and linewidths of the octahedral bending (320 cm^{-1}) and Jahn–Teller (480 cm^{-1}) modes changed discontinuously at 370 , 290 , and 235 K . In a normal anharmonic solid, the oscillator strength of the phonon mode is expected to be independent of the temperature^{39,48}. Moreover, at decreasing temperature, the phonon frequency should increase and the linewidth should decrease. The anharmonic dependence of the phonon frequency and linewidth is expressed as follows:

$$\omega(T) = \omega_0 + A \left(1 + \frac{2}{\exp\left(\frac{\Theta}{T}\right) - 1} \right) \quad (1)$$

$$\gamma(T) = \gamma_0 + B \left(1 + \frac{2}{\exp\left(\frac{\Theta}{T}\right) - 1} \right) \quad (2)$$

where ω_0 is the intrinsic frequency of the optical phonon mode, γ_0 is the linewidth broadening caused by defects, Θ is the Debye temperature, and A and B are the anharmonic coefficients⁴⁹. This model was used to get the best fit of the frequency and linewidth for temperatures above the magnetic ordering (235 K). For the octahedral bending mode at 327 cm^{-1} , the following values were obtained: $\omega_0 \approx 332.1 \text{ cm}^{-1}$, $\gamma_0 \approx 9.3 \text{ cm}^{-1}$, $A \approx -9 \text{ cm}^{-1}$, and $B \approx 5 \text{ cm}^{-1}$. For the Jahn–Teller mode at 482 cm^{-1} , the following values were obtained: $\omega_0 \approx 497 \text{ cm}^{-1}$, $\gamma_0 \approx 18.7 \text{ cm}^{-1}$, $A \approx -10.7 \text{ cm}^{-1}$, and $B \approx 7.6 \text{ cm}^{-1}$. The average Debye temperature was 478 K. The negative sign for A indicated that the phonon frequency increased as temperature decreased. The positive sign for B indicated that the linewidth decreased with a decrease in the temperature. The thin solid lines in Fig. 5 represent the theoretical predictions based on Eqs. (1) and (2) which describes the best fit line of the frequencies and linewidth above the magnetic ordering temperature (235 K). The octahedral bending mode at 327 cm^{-1} and the Jahn–Teller mode at 482 cm^{-1} deviated from the usual anharmonic contribution to the temperature dependence of the phonon frequency and linewidth because of the structural phase transition at 370 K, metal–insulator transition at 290 K, and antiferromagnetic ordering transition at 235 K. The deviation observed in the high-temperature phase could be attributed to the structural phase transition from tetragonal to orthorhombic symmetry at 370 K, anomalies in the lattice constant, and an increase in the Jahn–Teller distortions at 290 K²⁶. However, $\text{NdBaMn}_2\text{O}_6$ exhibited no drastic changes in its crystal structure and lattice constants in the low-temperature phase. The phonon anomalies at 235 K were most likely caused by spin–phonon interactions. The shoulder phonon peak appeared at approximately 440 cm^{-1} together with the enhancement of the 270 cm^{-1} phonon peak for a temperature lower than the metal–insulator transition temperature of 290 K. These phonon modes were likely activated by orthorhombic distortion because the $Cmmm$ structure was modified to the $P2_1am$ structure, which has lower orthorhombic symmetry. These phonon behaviors were directly correlated with the onset of the charge/orbital ordering, which was observed in $\text{NdBaMn}_2\text{O}_6$ at 290 K²⁵. The rotational distortion (270 cm^{-1}) accompanied with the Jahn–Teller octahedral distortions (440 cm^{-1}) was accounted to induce this ordering¹³.

The temperature evolution of the breathing mode at approximately 610 cm^{-1} is illustrated in Fig. 6. A third breathing mode at approximately 700 cm^{-1} was added in fitting from 20 K up to 60 K to accurately demonstrate the normal anharmonic linewidth behavior of the other breathing modes. We do not focus on this phonon mode because of its very weak intensity. The phonon associated with completely symmetrical oxygen stretching vibrations gradually red-shifted when the temperature decreased from 235 to 20 K. The other breathing mode near 660 cm^{-1} exhibited similar behavior. This softening is associated with the renormalization of the phonon induced by magnetic ordering, which is a signature of spin–phonon coupling. A similar softening for the 601 cm^{-1} was observed for NdMnO_3 which also exhibit an A type antiferromagnetism at low temperature. By contrast, the 607 cm^{-1} mode in $\text{Nd}_{0.5}\text{Sr}_{0.5}\text{MnO}_3$ which appears with the occurrence of the CE type antiferromagnetism temperatures shows a hardening to 610 cm^{-1} when temperature was lowered. No detailed analysis of the breathing mode was reported for $\text{SmBaMn}_2\text{O}_6$ ¹⁰ which also exhibits CE type antiferromagnetism. This behavior confirms the sensitivity of the spin–phonon coupling to the spin ordering^{42,45,46}.

The observed phonon softening correlated well with the normalized square of magnetic susceptibility data measured for $\text{NdBaMn}_2\text{O}_6$ ²⁶, as illustrated in Fig. 6(b). The spin–phonon contribution was caused by the modulation of the exchange integral through lattice vibrations, which is predicted in the mean field theory³⁹. Thus, in a simple model, the shift in phonon frequency caused by magnetic ordering is given as follows:

$$\Delta\omega(T) \approx \lambda \langle S_i \cdot S_j \rangle \approx 6\lambda \left(\frac{M(T)}{M_s} \right)^2 \quad (3)$$

where $\Delta\omega(T)$ is the shift in phonon frequency, λ is the spin–phonon coupling constant, and $\langle S_i \cdot S_j \rangle$ is the nearest neighbor spin correlation. The $\langle S_i \cdot S_j \rangle$ can be estimated from $6 \left(\frac{M(T)}{M_s} \right)^2$ where $M(T)$ is the magnetization per magnetic ion, M_s is the saturation magnetization and a factor of 6 considering the number of nearest neighbor^{39,46,50,51}. In the present study, we used the magnetic susceptibility with the external magnetic field along the ab plane. We estimated the renormalization of the phonon frequency due to the spin–phonon interaction by subtracting the anharmonic contributions, which can be estimated from the high temperature phonon frequencies. In this regard, we neglected the lattice effects and used the data at 260 K as the reference since the breathing mode becomes too weak and broad to be clearly resolved at higher temperature. Also, from the fitting results of the breathing modes at 260 K it can be observed that the phonon frequency still exhibits softening above the magnetic ordering temperature. This is caused by the in plane ferromagnetic correlations that exists in this temperature range²⁷. In addition, Raman scattering spectra in the breathing modes region do not change significantly at the high temperature phase where structural phase transition occurs. These results further justifies that the spin–phonon interaction plays a more important role in the softening of this mode rather than the lattice

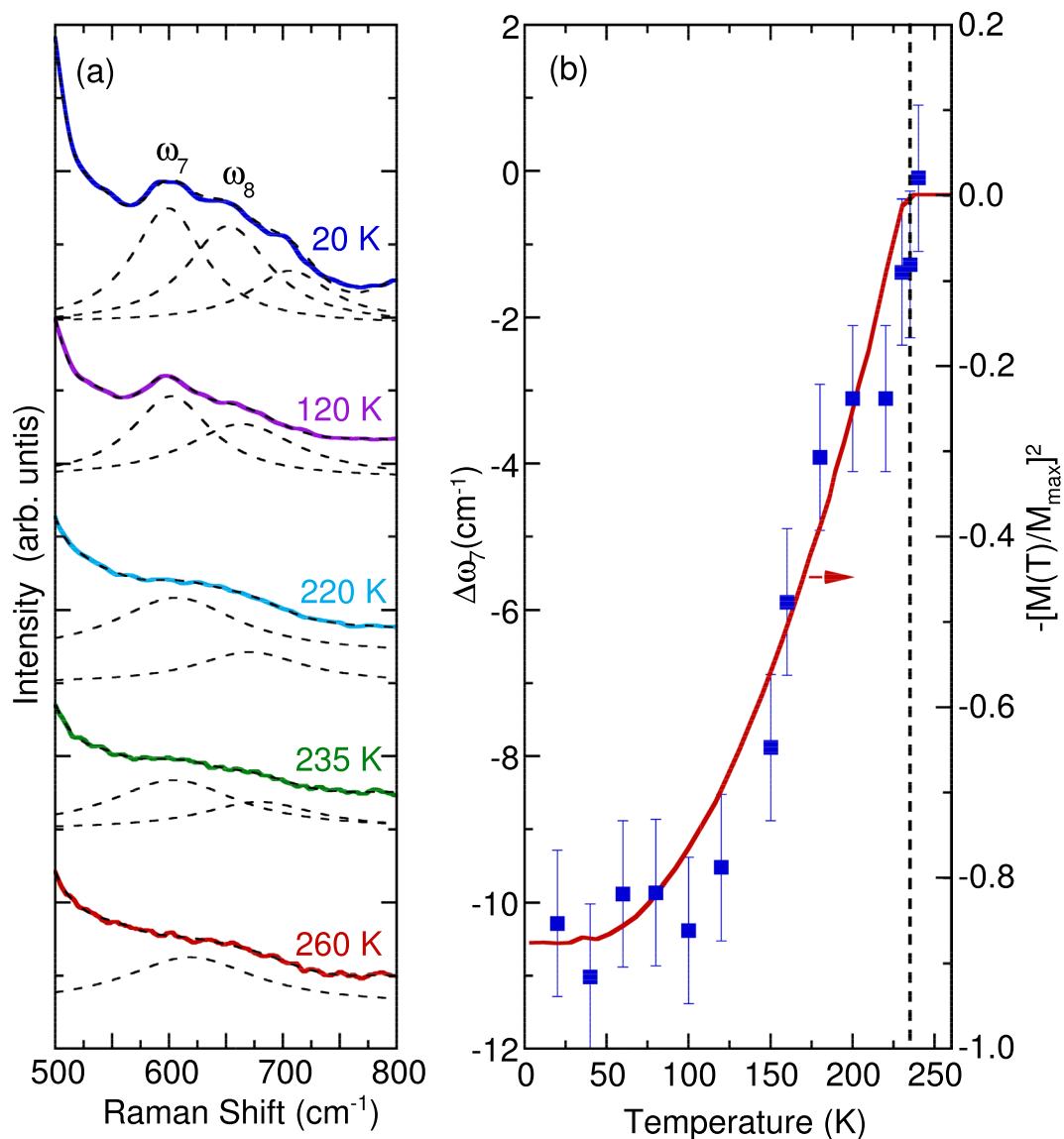


Figure 6. (a) Temperature dependence of the Raman scattering spectra between 500 and 800 cm^{-1} . The dashed lines indicate the best fit with the Lorentzian model. (b) Temperature dependence of the shift in the phonon frequency of the breathing mode (with respect to its value at 260 K) plotted against the normalized square of the magnetic susceptibility²⁶.

contributions. From Eq. (3) and the data from Fig. 6, the spin-phonon coupling constant was estimated to be $\lambda = 2.5 \text{ cm}^{-1}$.

A quantitative value of λ can also be obtained using a simplified lattice model proposed by Sushkov *et al.*⁵² which is given as follows:

$$\lambda \approx \frac{2\alpha^2 J}{m\omega} \quad (4)$$

where m is the mass of the magnetic ion, ω the mode frequency, J the nearest neighbor exchange coupling constant, and α can be calculated using $\alpha = 2z/3a_B$ (a_B is the Bohr radius and z is the nearest neighbor coordination number). Considering only the nearest neighbors ($z = 6$), we obtained $\alpha = 7.56/\text{\AA}$. Meanwhile, we estimated the exchange coupling constant using

$$J = 3k_B\Theta_{cw}/zS(S + 1) \quad (5)$$

where k_B is the Boltzmann constant, Θ_{cw} is the Currie-Weiss temperature, and S is the spin angular momentum^{52,53}. Here, we used $z = 6$, $S = 7/4$ and $\Theta_{cw} = 235 \text{ K}$ taken from ref. ²⁵ to get $J = 2.1 \text{ meV}$. Thus, we get the spin-phonon coupling constant $\lambda \approx 2 \text{ cm}^{-1}$ which is close to our obtained value of $\lambda = 2.5 \text{ cm}^{-1}$. These values are comparable to perovskite manganites and magnetic oxide materials in other studies^{39,52-56}.

Summary

We used spectroscopic ellipsometry and Raman scattering spectroscopy to determine the electronic structure and lattice dynamics of NdBaMn₂O₆ single crystals. The room-temperature optical absorption spectrum of NdBaMn₂O₆ indicated the occurrence of *d*–*d* on-site transitions in Mn at approximately 0.88 eV. The spectrum also indicated the occurrence of charge-transfer transitions between the 2*p* state of O and 3*d* of Mn at approximately 4.10 eV. The temperature dependent peak energy and intensity of the *d*–*d* excitation presented anomalies at 290 and 235 K. The octahedral bending mode at 327 cm^{−1} and Jahn–Teller mode at 482 cm^{−1} indicated the sensitivity of the single crystals to the structural phase transition at 370 K, metal–insulator transition at 290 K, and antiferromagnetic ordering transition at 235 K. Moreover, the activated phonon mode, which appeared at approximately 440 cm^{−1} alongside with the enhancement of the 270 cm^{−1} phonon mode, coupled strongly to the metal–insulator transition at 290 K, which was associated with charge/orbital ordering. The temperature dependence of the breathing mode at 610 cm^{−1} exhibited an anomalous softening at a temperature less than 235 K. The spin–phonon coupling constant obtained was $\lambda = 2.5 \text{ cm}^{-1}$ which is close to the calculated value of $\lambda \approx 2 \text{ cm}^{-1}$. These results confirmed a strong interaction among the charge, orbital, and spin degrees of freedom in NdBaMn₂O₆.

Received: 20 April 2019; Accepted: 20 September 2019;

Published online: 03 December 2019

References

- Ueda, Y. & Nakajima, T. The A-site ordered manganese perovskite and its colossal magnetoresistance. *Prog. Solid State Chem.* **35**, 397 (2007).
- Loktev, V. M. & Pogorelov, Y. G. Peculiar physical properties and the colossal magnetoresistance of manganites (Review). *Low Temp. Phys.* **26**, 171 (2000).
- Kézsmárki, I. *et al.* Optical phase diagram of perovskite colossal magnetoresistance manganites near half doping. *Phys. Rev. B - Condens. Matter Mater. Phys.* **77**, 075117 (2008).
- Moritomo, Y., Asamitsu, A., Kuwahara, H. & Tokura, Y. Giant magnetoresistance of manganese oxides with a layered perovskite structure. *Nature* **380**, 141 (1996).
- Basov, D. N., Averitt, R. D., van der Marel, D., Dressel, M. & Haule, K. Electrodynamics of correlated electron materials. *Rev. Mod. Phys.* **83**, 471 (2011).
- Rybicki, D., Sikora, M., Przewoznik, J., Kapusta, C. & Mitchell, J. F. Interplay of local structure, charge, and spin in bilayered manganese perovskites. *Phys. Rev. B* **97**, 115158 (2018).
- Saad H.-E, M. M. & Rammeh, N. Crystal structure, electronic and magnetic properties of double perovskite Ba₂FeWO₆: A combined experimental-theoretical study. *Phys. B Condens. Matter* **481**, 217 (2016).
- Serrate, D., De Teresa, J. M. & Ibarra, M. R. Double perovskites with ferromagnetism above room temperature. *J. Phys. Condens. Matter* **19**, 023201 (2007).
- Tokura, Y. & Nagaosa, N. Orbital physics in transition metal oxides. *Science* **288**, 462 (2000).
- Tomioka, Y. *et al.* Charge/orbital ordering in perovskite manganites. *J. Alloys Compd.* **326**, 27 (2001).
- Wang, Y. *et al.* High temperature metal-insulator transition induced by rare-earth doping in perovskite CaMnO₃. *J. Phys. Chem. C* **113**, 12509 (2009).
- Zhou, J. S. & Goodenough, J. B. Local structural distortions, orbital ordering, and ferromagnetism in underdoped La_{1-x}Sr_xMnO₃. *Phys. Rev. B* **91**, 064414 (2015).
- Li, J. Q. Structural properties of the perovskite manganites. *J. Appl. Phys.* **90**, 637 (2001).
- Caignaert, V., Millange, F., Domengès, B., Raveau, B. & Suard, E. A new ordered oxygen-deficient manganite perovskite: LaBaMn₂O_{5.5} crystal and magnetic structure. *Chem. Mater.* **11**, 930 (1999).
- Millange, F., Caignaert, V., Domengès, B., Raveau, B. & Suard, E. Order-disorder phenomena in new LaBaMn₂O_{6-x} CMR perovskites: crystal and magnetic structure. *Chem. Mater.* **10**, 1974 (1998).
- Arima, T. *et al.* Change in charge and orbital alignment upon antiferromagnetic transition in the A-site-ordered perovskite manganese oxide RBaMn₂O₆. *Phys. Rev. B* **66**, 140408 (2002).
- Akahoshi, D. *et al.* Random potential effect near the bicritical region in perovskite manganites as revealed by comparison with the ordered perovskite analogs. *Phys. Rev. Lett.* **90**, 177203 (2003).
- Nakajima, T., Yoshizawa, H. & Ueda, Y. A-site randomness effect on structural and physical properties of Ba-based perovskite manganites. *J. Phys. Soc. Japan* **73**, 2283 (2004).
- Nakajima, T., Kageyama, H., Yoshizawa, H. & Ueda, Y. Structures and electromagnetic properties of new metal-ordered manganites: RBaMn₂O₆ (R = Y and rare-earth elements). *J. Phys. Soc. Japan* **71**, 2843 (2002).
- Nakajima, T. & Ueda, Y. Structures and electromagnetic properties of the A-site disordered Ba-based manganites; R_{0.5}Ba_{0.5}MnO₃ (R = Y and rare earth elements). *J. Alloys Compd.* **383**, 135 (2004).
- Akahoshi, D. *et al.* Charge-orbital ordering near the multicritical point in A-site ordered perovskites SmBaMn₂O₆ and NdBaMn₂O₆. *Phys. Rev. B* **70**, 064418 (2004).
- Nakajima, T., Kageyama, H., Yoshizawa, H., Ohoyama, K. & Ueda, Y. Ground state properties of the A-site ordered manganites, RBaMn₂O₆ (R = La, Pr and Nd). *J. Phys. Soc. Japan* **72**, 3237 (2003).
- Zhang, Q., Guillou, F., Wahl, A., Bfard, Y. & Hardy, V. Coexistence of inverse and normal magnetocaloric effect in A-site ordered NdBaMn₂O₆. *Appl. Phys. Lett.* **96**, 242506 (2010).
- Yamada, S. *et al.* Room-temperature low-field colossal magneto-reistance in double-perovskite manganite, Retrieved from <http://arxiv.org/abs/1811.07596>.
- Aliev, A. M., Gamzatov, A. G., Kalitka, V. S. & Kaul, A. R. Low field magnetocaloric effect and heat capacity of A-site ordered NdBaMn₂O₆ manganite. *Solid State Commun.* **151**, 1820 (2011).
- Yamada, S. *et al.* Physical properties and crystal structure analysis of double-perovskite NdBaMn₂O₆ by using single crystals. *Phys. Rev. B* **95**, 035101 (2017).
- Yamada, S., Sagayama, H., Sugimoto, K. & Arima, T. Successive phase transitions and magnetic fluctuation in a double-perovskite NdBaMn₂O₆ single crystal. *J. Phys. Conf. Ser.* **969**, 012103 (2018).
- Momma, K. & Izumi, F. VESTA: a three-dimensional visualization system for electronic and structural analysis. *J. Appl. Crystallogr.* **41**, 653 (2008).
- Noh, T. W. W. *et al.* Infrared and Raman selection rules for lattice vibrations: the correlation method. *J. Korean Phys. Soc.* **36**, 392 (2000).
- Lee, H. J. *et al.* Optical properties of a Nd_{0.7}Sr_{0.3}MnO₃ single crystal. *Phys. Rev. B* **60**, 5251 (1999).
- Kaplan, S. G. *et al.* Optical evidence for the dynamic Jahn-Teller effect in Nd_{0.7}Sr_{0.3}MnO₃. *Phys. Rev. Lett.* **77**, 2081 (1996).
- Millis, A. J., Shraiman, B. I. & Mueller, R. Dynamic Jahn-Teller effect and colossal magnetoresistance in La_{1-x}Sr_xMnO₃. *Phys. Rev. Lett.* **77**, 175 (1996).

33. Liu, H. L. *et al.* Magneto-optical properties of $\text{La}_{0.7}\text{Sr}_{0.3}\text{MnO}_3$ thin films with perpendicular magnetic anisotropy. *J. Appl. Phys.* **99** (2006).
34. Arima, T., Tokura, Y. & Torrance, J. B. Variation of optical gaps in perovskite-type 3d transition-metal oxides. *Phys. Rev. B* **48**, 17006 (1993).
35. Jung, J. H. *et al.* Determination of electronic band structures of CaMnO_3 and LaMnO_3 using optical-conductivity analyses. *Phys. Rev. B* **55**, 15489 (1997).
36. Fateley, W. G., McDevitt, N. T. & Bentley, F. F. Infrared and Raman selection rules for lattice vibrations: The correlation method. *Appl. Spectrosc.* **25**, 155 (1971).
37. Abrashev, M. V. *et al.* Raman spectroscopy of CaMnO_3 : mode assignment and relationship between Raman line intensities and structural distortions. *Phys. Rev. B - Condens. Matter Mater. Phys.* **65**, 184301 (2002).
38. Iliiev, N. *et al.* Raman active phonons in orthorhombic YMnO_3 and LaMnO_3 . *J. Phys. Chem. Solids* **59**, 1982 (1998).
39. Granado, E. *et al.* Magnetic ordering effects in the Raman spectra of $\text{La}_{1-x}\text{Mn}_{1-x}\text{O}_3$. *Phys. Rev. B* **60**, 11879 (1999).
40. Silva, R. X. *et al.* Spin-phonon coupling in multiferroic Y_2CoMnO_6 . *J. Alloys Compd.* **690**, 909 (2017).
41. Silva, R. X. *et al.* Spin-phonon coupling in $\text{Gd}(\text{Co}_{1/2}\text{Mn}_{1/2})\text{O}_3$ perovskite. *J. Appl. Phys.* **114**, 194102 (2013).
42. Asselin, S. *et al.* Resonant micro-Raman study of $\text{Nd}_{0.5}\text{Sr}_{0.5}\text{MnO}_3$. *J. Phys. Condens. Matter* **17**, 5247 (2005).
43. Abrashev, M. V. *et al.* Raman spectroscopy of the charge- and orbital-ordered state in $\text{La}_{0.5}\text{Ca}_{0.5}\text{MnO}_3$. *Phys. Rev. B - Condens. Matter Mater. Phys.* **64**, 144429 (2001).
44. Granado, E., Sanjurjo, J. A., Rettori, C., Neumeier, J. J. & Oseroff, S. B. Order-disorder in the Jahn-Teller transition of LaMnO_3 : A Raman scattering study. *Phys. Rev. B - Condens. Matter Mater. Phys.* **62**, 11304 (2000).
45. Choi, K.-Y. *et al.* Raman scattering study of $\text{Nd}_{1-x}\text{Sr}_x\text{MnO}_3$ ($x = 0.3, 0.5$). *J. Phys. Condens. Matter* **15**, 3333 (2003).
46. Iliiev, M. N. *et al.* Raman spectroscopy of ordered double perovskite $\text{La}_2\text{CoMnO}_6$. *Phys. Rev. B* **75**, 104118 (2007).
47. Wang, W.-R., Xu, D.-P. & Su, W.-H. Raman shift in RMnO_3 ($R = \text{La, Pr, Nd, Sm}$) manganites, Chinese. *Phys. Lett.* **22**, 705 (2005).
48. Iliiev, M. N., Abrashev, M. V., Popov, V. N. & Hadjiev, V. G. Role of Jahn-Teller disorder in Raman scattering of mixed-valence manganites. *Phys. Rev. B - Condens. Matter Mater. Phys.* **67**, 212301 (2003).
49. Balkanski, M., Wallis, R. F. & Haro, E. Anharmonic effects in light scattering due to optical phonons in silicon. *Phys. Rev. B* **28**, 1928 (1983).
50. Macedo Filho, R. B. *et al.* Role of rare-earth ionic radii on the spin-phonon coupling in multiferroic ordered double perovskites. *Mater. Res. Express* **2**, 075201 (2015).
51. Pandey, P. K., Choudhary, R. J., Mishra, D. K., Sathe, V. G. & Phase, D. M. Signature of spin-phonon coupling in Sr_2CoO_4 thin film: A Raman spectroscopic study. *Appl. Phys. Lett.* **102**, 142401 (2013).
52. Laverdière, J. *et al.* Spin-phonon coupling in orthorhombic RMnO_3 ($R = \text{Pr, Nd, Sm, Eu, Gd, Tb, Dy, Ho, Y}$): A Raman study. *Phys. Rev. B - Condens. Matter Mater. Phys.* **73**, 214301 (2006).
53. Kumar, D., Kumar, S. & Sathe, V. G. Spin-phonon coupling in ordered double perovskites A_2CoMnO_6 ($A = \text{La, Pr, Nd}$) probed by micro-Raman spectroscopy. *Solid State Commun.* **194**, 59 (2014).
54. Elsässer, S., Geurts, J., Mukhin, A. A. & Balbashov, A. M. Lattice dynamics and spin-phonon coupling in orthorhombic $\text{Eu}_{1-x}\text{Ho}_x\text{MnO}_3$ ($x = 0.3$) studied by Raman spectroscopy. *Phys. Rev. B* **93**, 054301 (2016).
55. Sushkov, A. B., Tchernyshyov, O., Ratcliff, W., Cheong, S. W. & Drew, H. D. Probing spin correlations with phonons in the strongly frustrated magnet ZnCr_2O_4 . *Phys. Rev. Lett.* **94**, 137202 (2005).
56. Lee, S. H., Broholm, C., Kim, T. H., Ratcliff, W. & Cheong, S. W. Local spin resonance and spin-peierls-like phase transition in a geometrically frustrated antiferromagnet. *Phys. Rev. Lett.* **84**, 3718 (2000).

Acknowledgements

H.L.L. thanks financial support from the Ministry of Science and Technology of Republic of China under Grants No. MOST 108-2112-M-003-013 and Academia Sinica under thematic project Grant No. AS-105-TP-A03. S.Y. thanks financial support from Grant-in-Aid for Scientific Research (No. 24540380) of the Japan Society for the Promotion of Science and Strategic Research Promotion (No. G2503) of Yokohama City University.

Author contributions

H.L.L. and S.Y. conceived the idea and designed the experiments. R.D.M. performed the experiments. K.O. and S.Y. prepared the samples. R.D.M. and H.L.L. wrote the paper. All the authors discussed the results and commented on the manuscript.

Competing interests

The authors declare no competing interests.

Additional information

Supplementary information is available for this paper at <https://doi.org/10.1038/s41598-019-54524-0>.

Correspondence and requests for materials should be addressed to H.-L.L.

Reprints and permissions information is available at www.nature.com/reprints.

Publisher's note Springer Nature remains neutral with regard to jurisdictional claims in published maps and institutional affiliations.



Open Access This article is licensed under a Creative Commons Attribution 4.0 International License, which permits use, sharing, adaptation, distribution and reproduction in any medium or format, as long as you give appropriate credit to the original author(s) and the source, provide a link to the Creative Commons license, and indicate if changes were made. The images or other third party material in this article are included in the article's Creative Commons license, unless indicated otherwise in a credit line to the material. If material is not included in the article's Creative Commons license and your intended use is not permitted by statutory regulation or exceeds the permitted use, you will need to obtain permission directly from the copyright holder. To view a copy of this license, visit <http://creativecommons.org/licenses/by/4.0/>.

© The Author(s) 2019